Supplementary Materials

Molecular determinants of the factor VIII/von Willebrand factor complex revealed by BIVV001 cryo-electron microscopy

Short Title: Cryo-EM Structure of BIVV001

James R. Fuller,[1,2] Kevin E. Knockenhauer,[3] Nina C. Leksa,[3] Robert T. Peters,[3] Joseph D. Batchelor[1]

[1]Integrated Drug Discovery, Sanofi, Waltham, MA, USA
[2]Department of Biochemistry and Molecular Biology, University of Chicago, Chicago, IL, USA
[3]Rare Blood Disorders, Sanofi, Waltham, MA, USA

Contents

Supplemental Methods

Cryo-electron microscopy sample preparation and data processing

Information on the three data collection sessions are given in Supplemental Table 1. For plasma cleaning/glow discharge of the cryo-electron microscopy grids prior to sample application, the first dataset used an UltrAufoil 1.2/1.3 300 mesh grid (Quantifoil), which was plasma cleaned using a PELCO easiGlow operating at 25 mA for 75 seconds; the other two datasets used CFlat 1.2/1.3 400 gold mesh grids (Protochips) that were cleaned at the same amperage for 45 seconds.

In RELION, micrographs and their resulting particles were divided into groups based on the microscope image-shift settings used during their collection, because exposures on the two non-tilted grids were collected using beam-/image-shifts to move to data collection locations where possible. Downstream during contrast transfer function (CTF) refinement, parameters (beam-tilt, and trefoil/fourth order aberrations) were fit separately within these groups. In both CisTEM and RELION, particles were extracted within a box size of 384 pixels (407.04 Å). All three-dimensional (3D) masks used in RELION were created using the mask creations functions available within RELION and were based on low-pass filtering the map from most recent prior 3D refinement; in CisTEM, the user-free auto-masking method was enabled and used the BIVV001 molecular weight as input. Masks that excluded certain domains (VWF-D3 for much of the first part of the workflow, and the factor VIII A domains for partial signal subtraction) were created by manual editing of low-pass filtered maps using the tools available in UCSF Chimera. Between each of the significant steps described in the main text (3D classifications, per-particle motion correction, partial signal subtraction, and the final 3D refinement), one cycle of 3D refinement, CTF refinement (per-particle defocus, beam-tilt and trefoil), was performed in order to maximize the quality of the particle information available to the following step. Preceding the final 3D refinement that produced the map used for model building, CTF refinement also included fitting of fourth order aberrations. The final map sharpening B-factor was fitted by RELION to be -69.32 Å^2.

For the Fourier shell correlations (FSC) given in Supplemental Figure 2 and resolution estimates given in Supplemental Table 4, the map-model FSC was calculated using the method implemented in Phenix, assuming a conservative map resolution of 3.89 Å (the third quartile of per-voxel resolutions, as estimated by RELION). The global half-maps FSC was calculated using the phase-randomization corrected methods implemented in RELION. Directional half-maps FSCs were calculated using 3DFSC version 3.0 using default settings. All half-maps FSCs were calculated within the same mask used for the final 3D refinement.

Visualization

Figures were prepared using UCSF Chimera[1], UCSF ChimeraX[2], and PyMol[3].

Supplemental Figure Legends

Supplementary Figure 1. Cryo-EM data processing workflow. Following 2D classification and initial model refinement in CisTEM, CTF refinement was prioritized prior to 3D classification in Relion. This first 3D classification and subsequent per-particle motion correction ("particle polishing") greatly improved overall map quality for FVIII and VWF D′. Further 3D classification paired with partial signal subtraction was then used to find a particle subset that improved the FVIII C2 and VWF D3 density and produce the final map used for model building.

Supplementary Figure 2. Global and directional fourier shell correlation resolution estimates for the cryo-EM map. (A) The global half-map fourier shell correlation (FSC) (bold black trace) indicates an overall resolution of 2.9 Å at the gold-standard 0.143 threshold. Also given are the median (blue) and mean (green) directional FSC curves generated by the 3DFSC software. The shaded green area represents the spread of ± 1 standard deviation of directional FSCs around the mean. Values given in the figure legend denote where each trace crosses the 0.143 threshold, marked by the horizontal dashed grey line. **(B)** A histogram of the resolution estimates (at FSC = 0.143) for each directional FSC sampled. **(C)** The map-model FSC calculated by Phenix (red), with the global half-map FSC (black) repeated for reference. The map-model FSC crosses the FSC = 0.5 threshold at 3.0 Å.

Supplementary Figure 3. Angular particle distribution within the final cryo-EM map. Particle orientations from the final 3D refinement step, represented as a 3D histogram along the surface of a sphere. The corresponding orientation of the map is shown for reference. Two views are given, related by a 90° rotation around the vertical axis.

Supplementary Figure 4. Preferential position of BIVV001 Fc. (A) 2D class average of a BIVV001 side view where the Fc domain is not visible, due to flexibility. **(B)** 2D class average in the same orientation as A where the Fc domain is visible on the back side of FVIII, indicated by the red arrow.

Supplementary Figure 5. Cryo-EM potential map in low resolution regions corresponding to the FVIII C2 and VWF D3 domains. Insets show representative regions of the map and model from the FVIII C2 (left), VWF D3 (below), and FVIII A3 (right) domains. Only docking and automated refinement were used for modeling the FVIII C2 and VWF D3 domains. The FVIII A3 region, for comparison, permitted manual model building and refinement in addition to

automated methods. In the insets, the map is shown as grey mesh and the BIV001 model as sticks with carbons colored by domain as indicated. The source of the zoomed insets is marked on a global view of the map by black boxes and arrows. Two views of VWF D3 are given to highlight the map-model agreement around β-sheet secondary structure. The map shown was sharpened and filtered to local resolution.

Supplementary Figure 6. Cryo-EM potential map in the region around sulfated Y1680. The model is shown as sticks colored by element, with carbons colored according to domain as indicated.The map is shown as grey mesh. The map shown was sharpened and filtered to local resolution.

Supplementary Figure 7. FVIII a3 peptide forms a β-strand to cap the Til′ β-sheet in VWF D'. A close-up view of the three-stranded anti-parallel beta sheet formed between the Til′ region of VWF (red) and the FVIII a3 peptide (yellow) is shown.

Supplementary Movie 1. VWF-D3 rotates relative to VWF-D′. The movie begins with the VWF-D′D3 crystal structure super-imposed onto the BIVV001 structure via the D′ domain. The subsequent rotation shows the movement that VWF-D3 makes relative to VWF-D′ as a result of binding to FVIII. The movie ends with VWF-D3 positioned below the FVIII C domains as described for the cryo-EM structure of BIVV001.

References

1. Pettersen EF, Goddard TD, Huang CC, et al. UCSF Chimera--a visualization system for exploratory research and analysis. J Comput Chem. 2004;25(13):1605-1612.
2. Goddard TD, Huang CC, Meng EC, et al. UCSF ChimeraX: Meeting modern challenges in visualization and analysis. Protein Science. 2018;27(1):14-25.
3. Schrodinger, LLC. The PyMOL Molecular Graphics System, Version 1.8; 2015.

Supplemental Table 1

Details of cryo-EM data collection

Grid type	Micrograph/ exposure count*	Pixel size (Å/pixel)	Movie frames	Movie frame dose (e^-/Å2)	Total exposure dose (e^-/Å2)	Target defocus range (-µm)	Stage tilt (°)
UltrAufoil 1.2/1.3 300 mesh	756	1.06	30	1.3101	39.3017	1.2 – 2.6	0
CFlat 1.2/1.3 400 gold mesh	2551	1.06	30	1.3777	41.3297	1.2 – 2.3	0
CFlat 1.2/1.3 400 gold mesh	649	1.06	30	1.349	40.4697	1.2 – 2.1	30

*Count represents useable micrographs

Supplemental Table 2

Cryo-EM Data and Model Refinement Statistics

Data collection and processing	
Instrument	Titan Krios G2
Voltage (kV)	300 kV
Nominal magnification	81,000x
Camera	Gatan K3
Pixel size (Å)	1.06
Exposure dose	See Supplemental Table 1
Defocus range (μm)	
Micrographs, CTFFind	0.44 – 4.73
Per-particle, refined	0.40 – 4.99
Final particle images (no.)	116,200
Map and model validation	
Resolution (Å, masked)	
Half maps (FSC = 0.143)	2.91
Full map – Model (FSC = 0.5)	3.02
Masked model-map cross correlation	0.74
Model composition	
Protein residues	1678
Ligands	NAG: 5, BMA: 1, Zn: 1, Cu: 1, Ca: 2
Model ADP/B factors (Å^2)	
Protein mean (range)	32.19 (0.02 – 149.50)
Ligands mean (range)	24.41 (3.20 – 75.21)
Geometry R.M.S. deviations	
Bond lengths (Å) (no. outliers > 4σ)	0.003 (0)
Bond angles (°) (no. outliers > 4 σ)	0.554 (0)
Ramachandran angles	
Favored (%)	96.91
Allowed (%)	3.09
Outliers (%)	0.00
Peptide plane outliers (%)	
Cis (proline / general)	2.4 / 0.0
Twisted (proline / general)	0.0 / 0.0
Rotamer outliers (%)	0.13
Cβ outliers (%)	0.00
Clashscore	7.86
MolProbity score[1]	1.61
EMRinger score[2]	3.18

1. Williams CJ, Headd JJ, Moriarty NW, et al. MolProbity: More and better reference data for improved all-atom structure validation. *Protein Sci*. 2018;27(1):293-315.
2. Barad BA, Echols N, Wang RY, et al. EMRinger: side chain-directed model and map validation for 3D cryo-electron microscopy. Nat Methods. 2015;12(10):943-946.

Supplemental Table 3

Hemophilia A missense mutations identified in FVIII-VWF D'D3 interface

Interface	Interface residue	Mutation	Disease severity	Reported cases
FVIII a3-VWF D' (Til')	Phe1677	Val	Moderate	2
	Phe1677	Ser	Mild	
	Ile1679	Thr	Mild or moderate	8
	Tys1680	Cys	Mild or moderate	82
	Tys1680	Phe	Mild or moderate	
	Tys1680	Ser	Mild or moderate	
FVIII A3-VWF D' (Til')	Arg1696	Gly	Mild	12
	Arg1696	Gln	Mild	
	Arg1696	Pro	Moderate	
	Tyr1698	Cys	Mild or severe	3
	Phe1699	Leu	Mild	1
	Phe1738	Leu	Moderate	1
	Asp1740	Asn	Mild or moderate or severe	7
	Asp1740	His	Mild	
	Gln1745	Arg	Severe	1
	His1867	Asn	Mild	1
FVIII C1-VWF D3 (VWD3)	Arg2090	Cys	Mild	1
FVIII C1-VWF D' (Til')	Ser2099	Pro	Mild	2
	Ser2099	Phe	Severe	
	Gln2100	Glu	Severe	3
	Gln2100	Arg	Moderate or severe	
	Ile2102	Asn	Mild	1
	Arg2116	Gly	Mild or moderate	7
	Arg2116	Pro	Severe	
FVIII C1-FVIII a3 (Y1680)-VWF D' (Til')	Ser2119	Phe	Mild	4
	Ser2119	Tyr	Mild or moderate	
FVIII C1-VWF D' (Til')	Gly2121	Glu	Severe	1
	Thr2122	Asn	Severe	1
	Phe2127	Ser	Mild	34
	Gly2128	Ser	Mild	4
	Gly2128	Asp	Moderate or severe	
	Asn2129	Asp	Moderate or severe	28
	Asn2129	Ser	Mild or moderate	
FVIII C1-VWF D' (E')	Val2130	Gly	Moderate	1
	Asp2131	Val	Severe	1
	Ser2133	Pro	Mild	2
FVIII C1-VWF D' (Til')	Lys2136	Glu	Mild	3
	Arg2150	Cys	Mild	204
	Arg2150	His	Mild or moderate or severe	
	Arg2150	Leu	Mild	
	His2152	Tyr	Mild	5
	His2152	Arg	Moderate	
	Pro2153	Arg	Severe	6
	Pro2153	Gln	Mild or moderate	
	Pro2153	Leu	Severe	
	Thr2154	Ala	Mild or severe	8
	Thr2154	Asn	Mild	
	Thr2154	Ile	Mild	
	His2155	Asp	Mild or moderate	4
	His2155	Tyr	Mild	
	His2155	Arg	Severe	
	His2155	Pro	Severe	
	Ser2157	Arg	Mild	1
FVIII C2-VWF D3 (C8-3)	Met2199	Val	Severe	1
	Ala2201	Pro	Mild or moderate	27
	Thr2253	Pro	Mild	2

Source: EAHAD F8 variant database. http://f8-db.eahad.org/

Supplemental Table 4

VWD type 2N mutations in VWF-D'D3

Residue	Mutation	Interface with FVIII?	Location in VWF	FVIII contacting domain
Glu787	Lys	Y	D' (Til')	C1
Thr791	Met	Y	D' (Til')	C1
Met800	Val	Y	D' (Til')	C1
Pro812	Leu	N	D' (Til')	N/A
Arg816 Arg816	Trp Gln	Y	D' (Til')	a3
His817	Gln	Y	D' (Til')	C1
Arg854	Gln	N	D' (E')	N/A
Asp879*	Asn	N	D3 (VWD3)	N/A
Gln1053	His	Y	D3 (C8-3)	C2
Glu1078	Lys	Y	D3 (C8-3)	C2

Source: Dong et al. 2019 Blood *Also classified as type 2A

Supplemental Figure 1

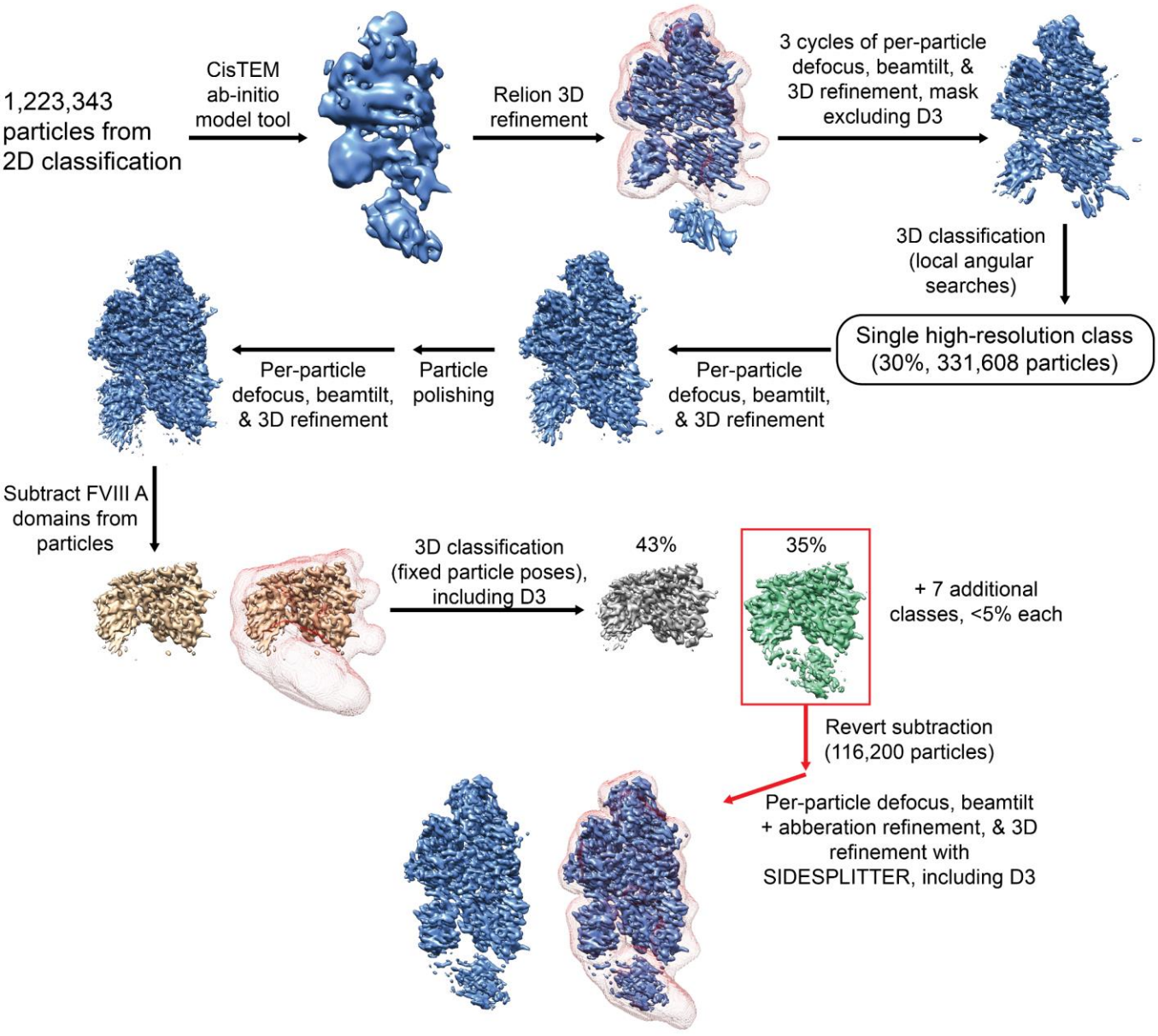

Supplemental Figure 2

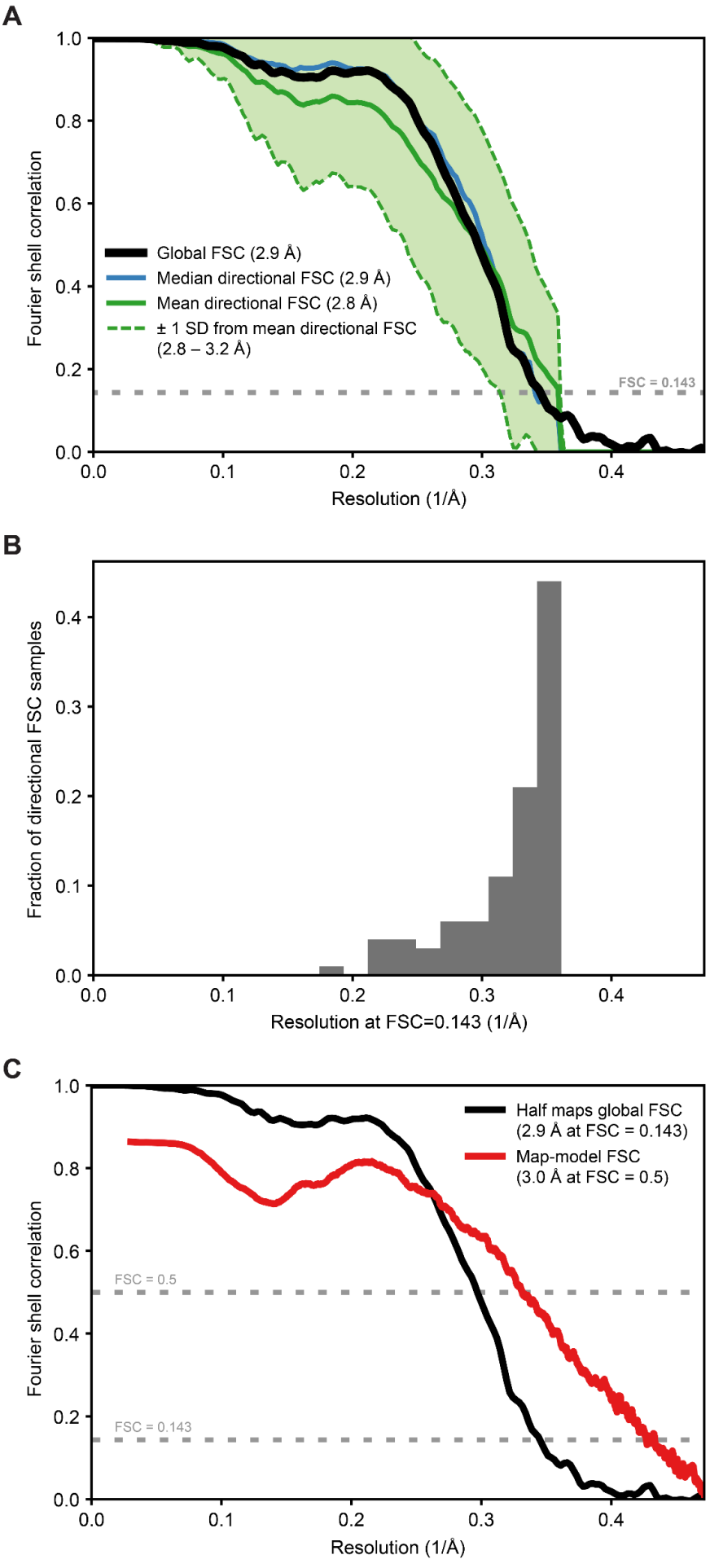

Supplemental Figure 3

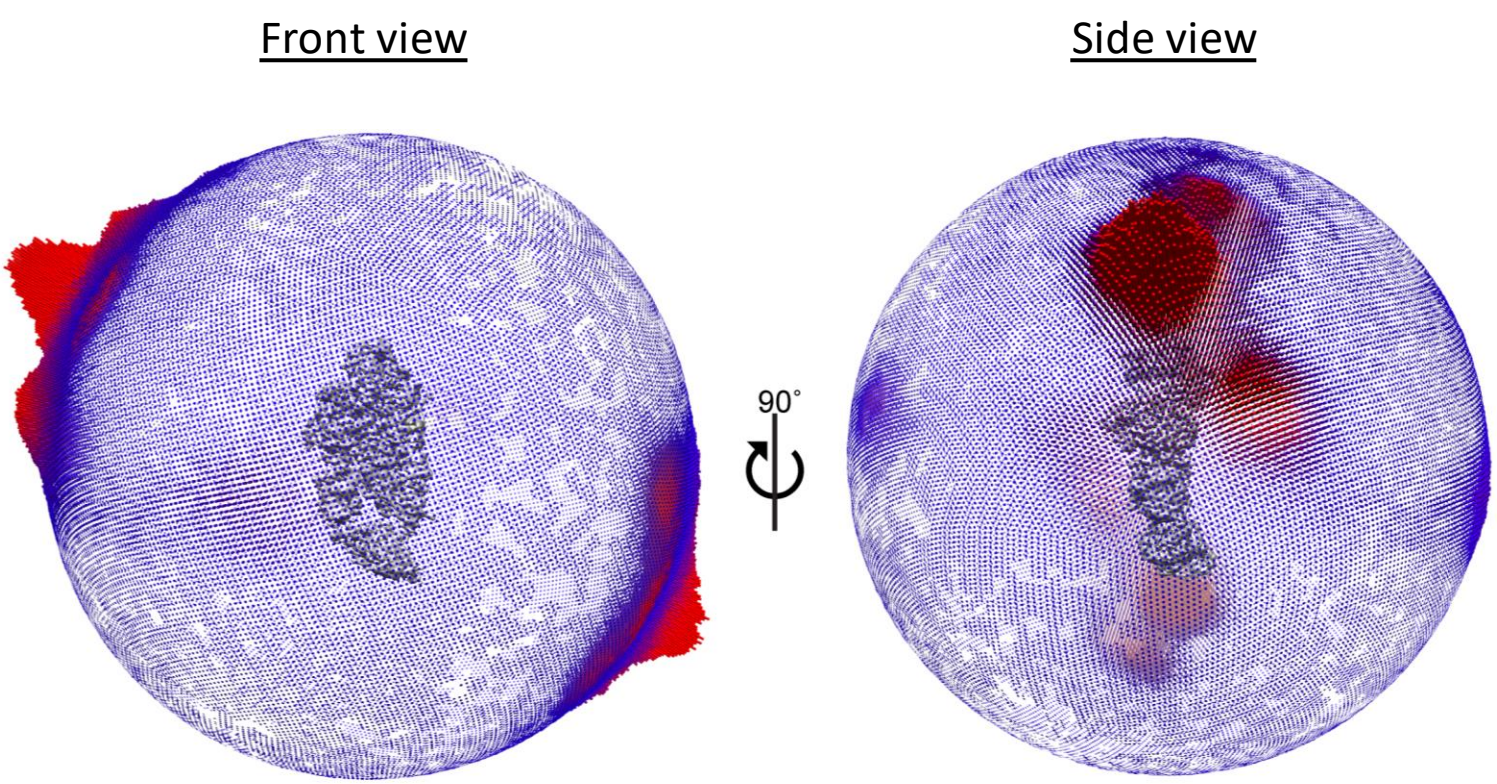

Supplemental Figure 4

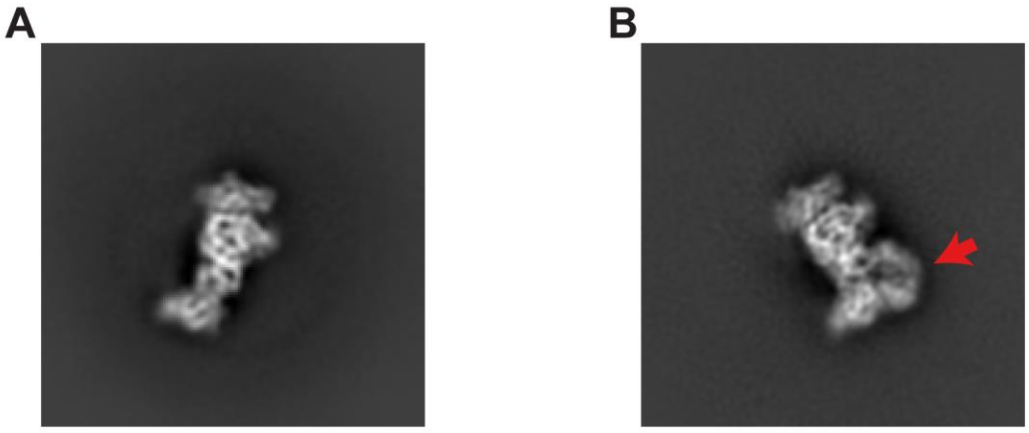

Supplemental Figure 5

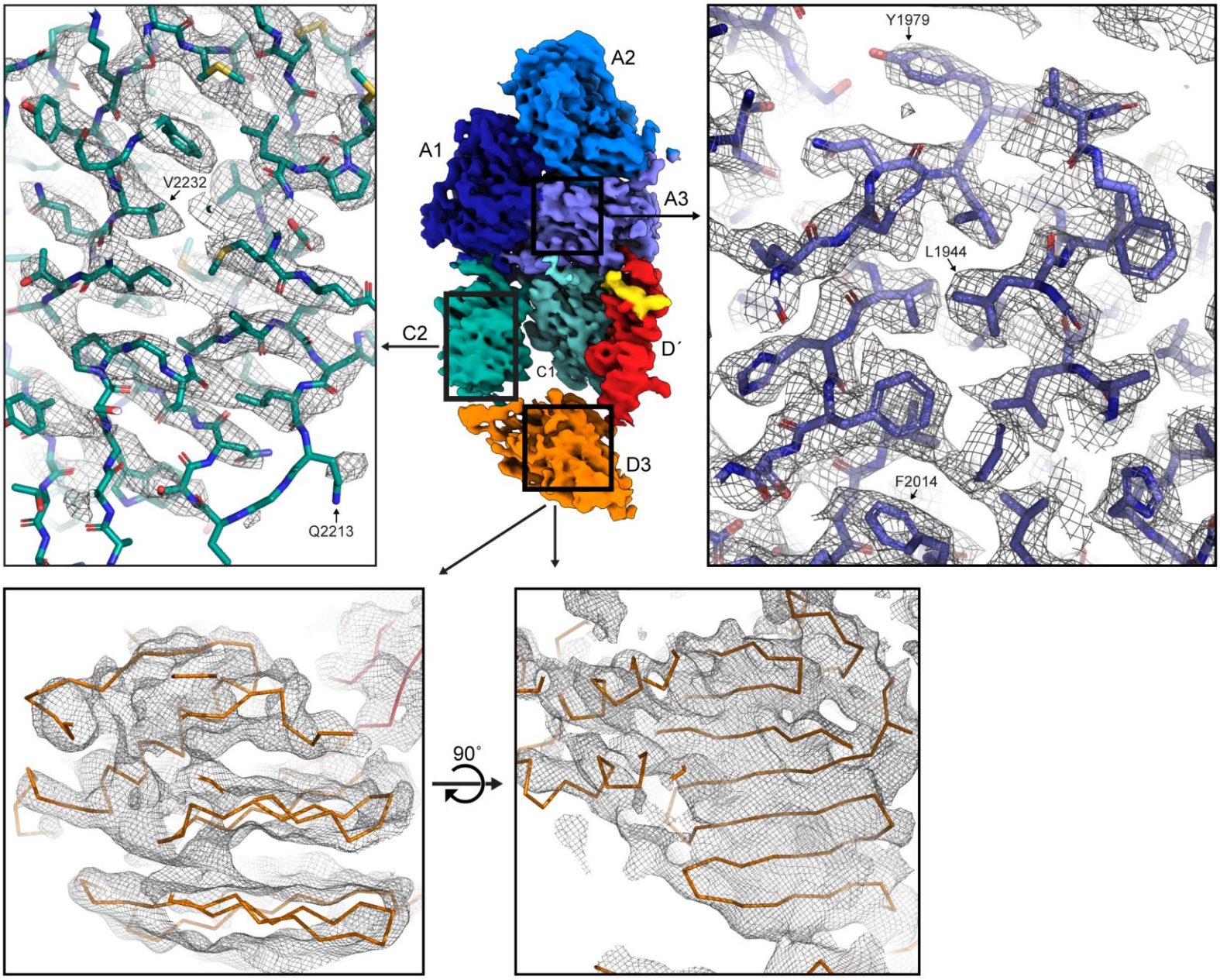

Supplemental Figure 6

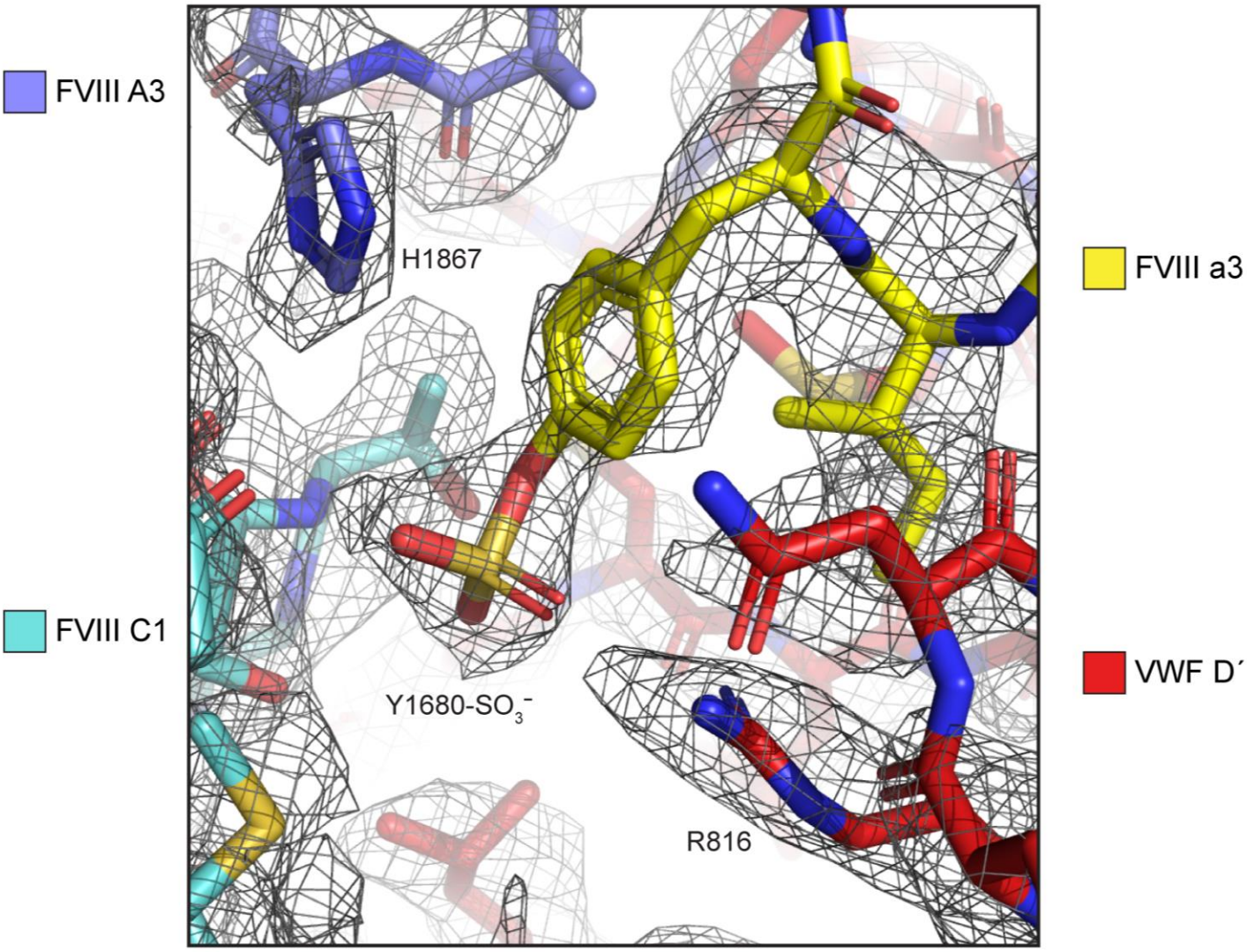

Supplemental Figure 7

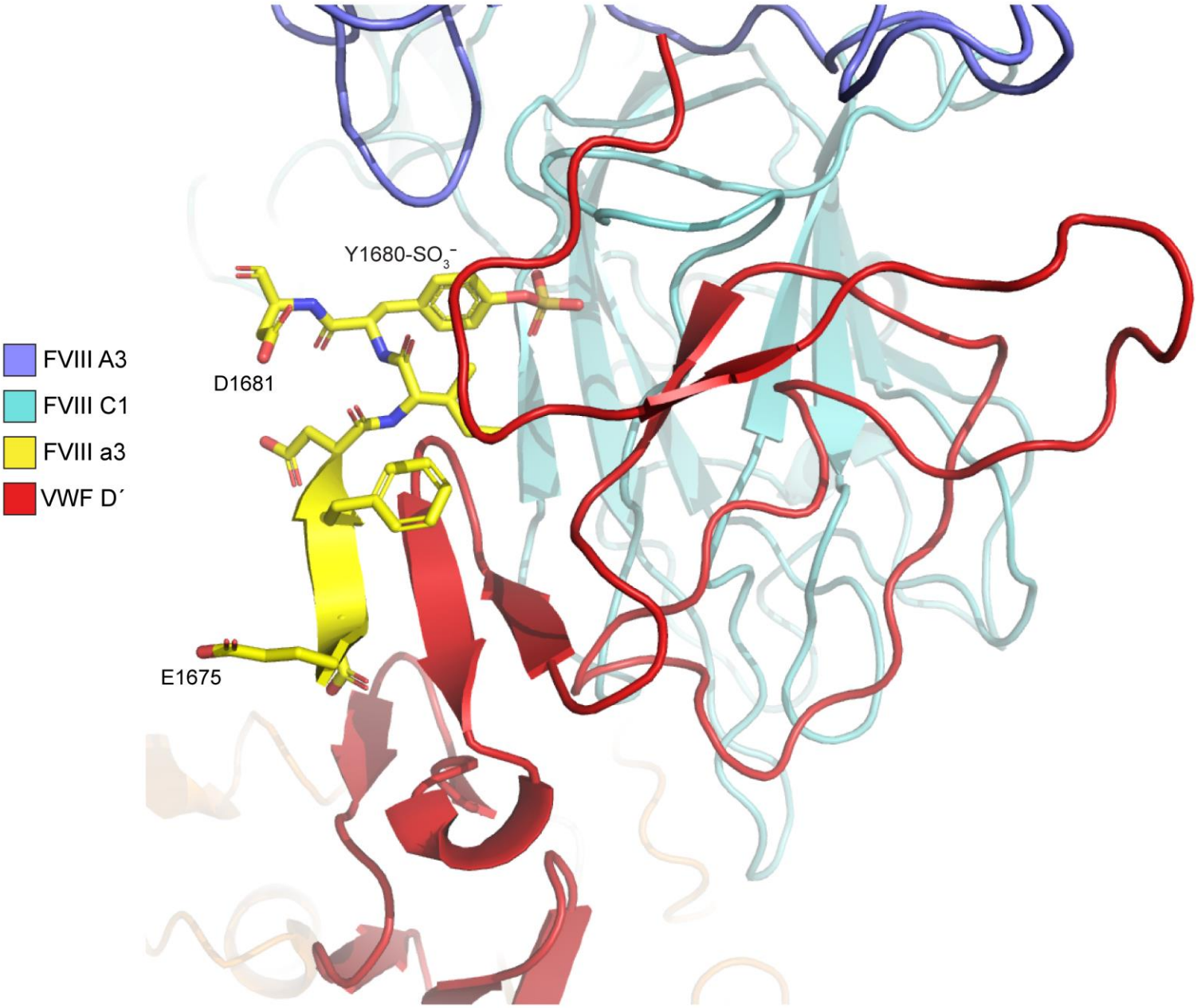

Supplemental Movie 1